VIII International Conference on Fracture Mechanics of Concrete and Concrete Structures
FraMCoS-8
J.G.M. Van Mier, G. Ruiz, C. Andrade, R.C. Yu and X.X. Zhang (Eds)

A VISCOELASTIC RETARDED DAMAGE MATERIAL LAW FOR CONCRETE STRUCTURES EXPOSED TO IMPACT AND EXPLOSIONS

ULRICH HÄUSSLER-COMBE AND TINO KÜHN

Institute of Concrete Structures
Technische Universität Dresden, 01062 Dresden, Germany
e-mail: Ulrich.Haeussler-Combe;Tino.Kuehn@tu-dresden.de, www.tu-dresden.de/biwitb/mbau/

Key words: Concrete, Retarded Damage, Strain-Rate Effect, Dynamic Strength Increase, Spallation

Abstract. The paper introduces a novel material model which includes the effects of dynamic strength increase of concrete. The model is based on the physical assumption of combined viscous effects and a retarded damage approach. Furthermore, this model is implemented in a Finite-Element-Method with implicit time integration and applied to numerical investigations of concrete bars exposed to impulse loading and wave propagation, respectively. Particular cases of direct tensile wave propagation and furthermore spallation of bars due to tensile failure are investigated with special respect to the dynamic tensile strength increase, dynamic failure mechanisms and crack energy.

1 INTRODUCTION

Strength of concrete may exceed quasistatic values in case of high strain-rates caused by high velocity loading such as impacts or explosions. This effect was experimentally validated in a number of experimental investigations [2], [9]. It may have a considerable influence on the behavior of concrete structures and lead to an increased dynamic load bearing capacity compared to the quasistatic case. While the so called lateral confinement may contribute to an increased compressive strength, the increase of tensile strength must be caused by physical mechanisms regarding the concrete's material structure. Two different physical phenomena are involved according to the current state of knowledge. While low strain rate effects are dominated by moisture and the movement of water in the different capillary systems of concrete [12], the damage at high strain rates appears to be dominated by inertia effects of micro-cracking [11], [4]. The micro-cracks cannot propagate arbitrarily fast as a displacement of internal crack faces relative to their immediate surrounding is involved. This leads to a retardation of crack propagation or retarded damage, respectively. A suitable framework is given with continuum mechanics and concepts of elasticity, viscosity, damage and plasticity. In order to compute the behavior of structures a macroscopic approach is appropriate.

A number of proposals have been published for stress-strain relations to incorporate the strain-rate effect. A majority modifies strength parameters as have been determined under quasistatic conditions by dynamic strength increase factors according to experimental results, see, e.g., [8]. These are phenomenological approaches and do not consider physical mechanisms. Approaches based on viscoelasticity or viscoplasticity have been proposed by, e.g. [1]. Direct modifications of damage parameters ruled by the strain-rate were proposed by, e.g., [14]. First concepts of retarded damage used in stress-strain relation were given by [4], [6].

The following paper bases upon the latter works and combines damaged viscoelasticity with a retardation of damage to develop a general triaxial material law including the strain-rate effect. A key point is given with the regularization of the softening material behavior with the gradient damage approach and its extension with respect to retarded damage.

The paper is organized as follows: Section 2 develops the material law as a an ordinary differential equation combining stress and strain and their rates. This is incorporated in a Finite-Element-Method combined with a Newmark-Method for temporal discretization as described in Section 3. It is applied to two particular cases of wave propagation: tensile wave propagation with continuously increasing loading in Section 4 and spallation with a moderate compressive amplitude reflecting as tensile wave in Section 5. Finally, some conclusions are given in Section 6

2 THE CONSTITUTIVE LAW

2.1 Quasistatic part

The constitutive law bases upon isotropic damaged elasticity

$$\boldsymbol{\sigma} = (1-D)\,\boldsymbol{E}\cdot\boldsymbol{\epsilon} \tag{1}$$

with the stress tensor $\boldsymbol{\sigma}$, the strain tensor $\boldsymbol{\epsilon}$, the linear isotropic elasticity tensor $\boldsymbol{E}$ with an initial Young's modulus E_0 and Poisson's ratio ν_0 as parameters. Scalar damage is measured by D with a condition $0 \le D \le 1$. Damage depends on a loading history. A strain based approach is chosen relating the strain state $\boldsymbol{\epsilon}$ with an equivalent damage strain κ by a relation $F(\boldsymbol{\epsilon},\kappa) = 0$. Furthermore, a relation $D = D(\kappa)$ connects damage D and the equivalent damage strain κ. Finally, Kuhn-Tucker conditions $F \le 0,\ \dot{D} \ge 0,\ \dot{D}\,F = 0$ with the time derivative $\dot{D}$ of D distinguish loading from unloading states. The exact forms of $F(\boldsymbol{\epsilon},\kappa), D(\kappa)$ are given in [5]. The approach introduces several material parameters beneath E_0, ν_0. These parameters rule nonlinear uniaxial stress-strain behavior and multiaxial strength properties.

The incremental form of Eq. (1) is given by

$$\dot{\boldsymbol{\sigma}} = (1-D)\,\boldsymbol{E}\cdot\dot{\boldsymbol{\epsilon}} - \dot{D}\,\boldsymbol{\sigma}_0, \quad \boldsymbol{\sigma}_0 = \boldsymbol{E}\cdot\boldsymbol{\epsilon} \tag{2}$$

with the time derivatives $\dot{\boldsymbol{\sigma}}, \dot{\boldsymbol{\epsilon}}, \dot{D}$ of $\boldsymbol{\sigma}, \boldsymbol{\epsilon}, D$. This is splitted into volumetric and deviatoric parts

$$\dot{\boldsymbol{\sigma}} = \dot{\boldsymbol{\sigma}}^{vol} + \dot{\boldsymbol{\sigma}}^{dev} \tag{3}$$

whereby

$$\begin{aligned} \dot{\boldsymbol{\sigma}}^{vol} &= K_0\left[(1-D)\dot{\boldsymbol{\epsilon}}^{vol} - \dot{D}\,\boldsymbol{\epsilon}^{vol}\right] \\ \dot{\boldsymbol{\sigma}}^{dev} &= 2G_0\left[(1-D)\dot{\boldsymbol{\epsilon}}^{dev} - \dot{D}\,\boldsymbol{\epsilon}^{dev}\right] \end{aligned} \tag{4}$$

with the initial bulk modulus and shear modulus

$$K_0 = \frac{E_0}{3(1-2\nu_0)}, \quad G_0 = \frac{E_0}{2(1+\nu_0)} \tag{5}$$

Due to $D = D(\kappa)$ the time derivative $\dot{D}$ is connected to the time derivative $\dot{\kappa}$ of the equivalent damage strain, which in turn is connected to $\dot{\boldsymbol{\epsilon}}$ by $\dot{F} = 0$ in case of loading [5].

2.2 Viscosity

The strain rate effect in the lower strain rate range is covered by a viscous approach. It is applied to the deviatoric part of Eq. (4). The general form for three parameter viscoelasticity is given by [10]

$$\dot{\boldsymbol{\sigma}}^{dev} = q_1\,\dot{\boldsymbol{\epsilon}}^{dev} + q_0\,\boldsymbol{\epsilon}^{dev} - p_0\,\boldsymbol{\sigma}^{dev} \tag{6}$$

The Maxwell model will be used in the following leading to coefficients

$$q_1 = 2(G_0+G_1), \quad q_0 = \frac{2G_0G_1}{\eta_1}, \quad p_0 = \frac{G_1}{\eta_1} \tag{7}$$

The shear modulus G_0 corresponds to Eq. (5). The shear modulus G_1 and the viscosity η_1 come into effect with larger strain rates. A high strain rate or high viscosity leads to a higher resulting shear stiffness temporarily approaching $G_0 + G_1$. The viscoelastic approach Eq. (6) is extended with

$$\begin{aligned} \dot{\boldsymbol{\sigma}}^{dev} = &(1-D)\,q_1\dot{\boldsymbol{\epsilon}}^{dev} - \dot{D}\,q_1\boldsymbol{\epsilon}^{dev} \\ &+(1-D)^2 q_0\boldsymbol{\epsilon}^{dev} - (1-D)p_0\boldsymbol{\sigma}^{dev} \end{aligned} \tag{8}$$

to describe damage. This particular form is chosen to include the quasistatic form Eq. (3) as a special case. The superposition with $\dot{\boldsymbol{\sigma}}^{vol}$ according to Eq. (4) is straightforward and leads to a relation for $\dot{\boldsymbol{\sigma}}$ depending on $\boldsymbol{\epsilon}, \dot{\boldsymbol{\epsilon}}, D, \dot{D}$ and furthermore on $\epsilon^{dev}, \boldsymbol{\sigma}^{dev}$.

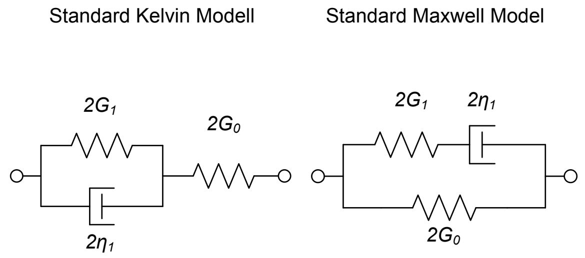

Figure 1: Three parameter models for viscoelasticity.

2.3 Gradient damage

A damage material law given by Eq. (1) is characterized by a maximum stress or strength, respetively, followed by a softening, i.e. decreasing stresses with increasing strains. This leads to localization phenomena within structures. Usage of such a law within numerical methods requires a regularization to avoid a fundamental mesh sensivity. The gradient damage approach will be used in the following. Thus, a nonlocal equivalent damage strain $\bar{\kappa}$ is employed within this setting which is related to the local equivalent strain κ by a differential equation

$$\bar{\kappa}(\boldsymbol{x}) - c_\kappa\, \Delta\bar{\kappa}(\boldsymbol{x}) = \kappa(\boldsymbol{x}), \quad c_\kappa = \frac{R^2}{2} \qquad (9)$$

with the Laplace differential operator Δ and a characteristic length R. A given field $\kappa(\boldsymbol{x})$ with highly localized values in a narrow band will lead to a field $\bar{\kappa}(\boldsymbol{x})$ localized in another band whose width is controlled by the value of R. Regarding the stress-strain law Eq. (1) of a material point in a position $\boldsymbol{x}$ the value $\bar{\kappa}$ replaces κ upon deriving damage D.

The parameter R is a measure of the material's heterogeneity and assumed as a material constant. An approximately linear relation can be derived between R and the crack energy G_f [6]. This is used to choose appropriate values for R.

Retardation of damage is assumed as another contribution to the strain rate effect beneath viscosity. This is modeled by an extension of Eq. (9) with an inertial like part with the second time dervative of the nonlocal equivalent strain $\ddot{\bar{\kappa}}$ and an mass-like parameter m_κ [6]

$$m_\kappa\, \ddot{\bar{\kappa}}(\boldsymbol{x}) + \bar{\kappa}(\boldsymbol{x}) - c_\kappa\, \Delta\bar{\kappa}(\boldsymbol{x}) = \kappa(\boldsymbol{x}) \qquad (10)$$

A model is given with Fig. 2 with a row of springs in parallel each with stochastically varying strength. This yields the uniaxial stress strain behavior with limited strength and subsequent softening. It is extended with inertial masses which sustain forces in a short time period in case of spring failure. This effect is ruled by the value of m_κ which is assumed as another material parameter for the strain rate effect beneath G_2, η_2.

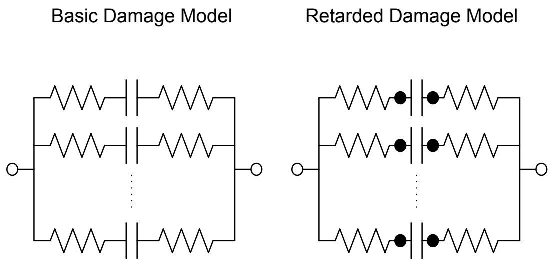

Figure 2: Models for damage and retarded damage.

3 THE NUMERICAL METHOD

Dynamic equilibrium of a structure is described by the virtual work principle

$$\begin{aligned} &\int_V \delta\boldsymbol{u}^T \cdot \ddot{\boldsymbol{u}}\, \rho \mathrm{d}V + \int_V \delta\boldsymbol{\epsilon}^T \cdot \boldsymbol{\sigma}\, \mathrm{d}V \\ &\quad = \int_V \delta\boldsymbol{u}^T \cdot \boldsymbol{b}\, \mathrm{d}V + \int_{A_t} \delta\boldsymbol{u}^T \cdot \boldsymbol{t}\, \mathrm{d}A \end{aligned} \qquad (11)$$

with the Cauchy stress $\boldsymbol{\sigma}$, body forces $\boldsymbol{b}$, specific mass ρ, acceleration $\ddot{\boldsymbol{u}}$, virtual displacements $\delta\boldsymbol{u}$, corresponding virtual strains $\delta\boldsymbol{\epsilon}$, surface tractions $\boldsymbol{t}$, the body's volume V and that part of surface A_t with prescribed tractions. Boundary conditions are defined as prescribed displacements $\boldsymbol{u}$ on surface part A_u and as surface tractions $\boldsymbol{t}$ on a surface part A_t.

This has to be complemented with a weak form for the differential equation (10) relating $\bar{\kappa}$ to κ. It is given by [6]

$$\begin{aligned} &\int_V \delta\bar{\kappa}\, \ddot{\bar{\kappa}}\;\; m_\kappa \mathrm{d}V + \int_V \delta\bar{\kappa}\, \bar{\kappa}\;\; \mathrm{d}V \\ &\quad + \int_V \nabla\delta\bar{\kappa} \cdot \nabla\bar{\kappa}\;\; c_\kappa \mathrm{d}V = \int_V \delta\bar{\kappa}\, \kappa\;\; \mathrm{d}V \end{aligned} \qquad (12)$$

with the nabla operator ∇ and a virtual variation $\delta\bar{\kappa}$. Boundary conditions for nonlocal fields are still on open research issue. According to a widely accepted approach a zero normal derivative $\boldsymbol{n} \cdot \nabla\bar{\kappa} = 0$ of the nonlocal equivalent damage strain is assumed.

Eqns (11,12) form a base to apply the Finite-Element-Method. The fields of displacements

$\boldsymbol{u}(\boldsymbol{x})$ and nonlocal equivalent damage strains $\bar{\kappa}(\boldsymbol{x})$ are used as independent variables. They are spatially discretized with

$$\begin{pmatrix} \boldsymbol{u}(\boldsymbol{x}) \\ \bar{\kappa}(\boldsymbol{x}) \end{pmatrix} = \boldsymbol{N}(\boldsymbol{x}) \cdot \boldsymbol{U} \tag{13}$$

with a matrix $\boldsymbol{N}(\boldsymbol{x})$ of shape functions and a vector $\boldsymbol{U}_I$ collecting nodal values of displacements and nonlocal equivalent strains. The spatial derivatives are given by

$$\begin{pmatrix} \boldsymbol{\epsilon}(\boldsymbol{x}) \\ \nabla\bar{\kappa}(\boldsymbol{x}) \end{pmatrix} = \boldsymbol{B}(\boldsymbol{x}) \cdot \boldsymbol{U} \tag{14}$$

with a matrix $\boldsymbol{B}(\boldsymbol{x})$ of nodal derivatives of shape functions. Applying standard methods of discretization on Eqns. (11,12) using Eqns. (13,14) leads to system of nonlinear ordinary differential equations of 2nd order depending on time t

$$\boldsymbol{M} \cdot \ddot{\boldsymbol{U}} + \boldsymbol{f}(\boldsymbol{U}) = \boldsymbol{p}(t) \tag{15}$$

with the generalized mass matrix $\boldsymbol{M}$, the acceleration $\ddot{\boldsymbol{U}}$ of nodal variables, the generalized internal nodal forces $\boldsymbol{f}$ nonlinearily depending on the nodal variables $\boldsymbol{U}$ and the nodal loads $\boldsymbol{p}$ depending on time t.

Temporal discretization of this system is performed with the implicit Newmark-Method. This requires the evaluation of the tangential stiffness [6]

$$\boldsymbol{K} = \frac{\partial \boldsymbol{f}}{\partial \boldsymbol{U}} \tag{16}$$

and leads to scheme

$$\begin{aligned} \tfrac{1}{\beta\Delta t^2}\boldsymbol{M} \cdot \left[\boldsymbol{U}^i - \hat{\boldsymbol{U}}^i\right] + \boldsymbol{K}^i \cdot \left[\boldsymbol{U}^i - \boldsymbol{U}^{i-1}\right] \\ = \boldsymbol{p}^i - \boldsymbol{f}^{i-1} \end{aligned} \tag{17}$$

with a time step Δt, a time $t^i = i\,\Delta t$, furthermore $\boldsymbol{U}^i = \boldsymbol{U}(t^i)$, $\boldsymbol{K}^i = \boldsymbol{K}(\boldsymbol{U}^i)$, $\boldsymbol{p}^i = \boldsymbol{p}(t^i)$, $\boldsymbol{f}^{i-1} = \boldsymbol{f}(t^{i-1})$ and

$$\hat{\boldsymbol{U}}^i = \boldsymbol{U}^{i-1} + \Delta t\ \dot{\boldsymbol{U}}^{i-1} \tag{18}$$

$$+\frac{\Delta t^2}{2}(1-2\beta)\,\ddot{\boldsymbol{U}}^{i-1} \tag{19}$$

$$\ddot{\boldsymbol{U}}^i = \frac{1}{\beta\Delta t^2}\left[\boldsymbol{U}^i - \hat{\boldsymbol{U}}^i\right] \tag{20}$$

$$\dot{\boldsymbol{U}}^i = \dot{\boldsymbol{U}}^{i-1} + \Delta t\Big[\gamma\ddot{\boldsymbol{U}}^i \tag{21}$$

$$+(1-\gamma)\ddot{\boldsymbol{U}}^{i-1}\Big] \tag{22}$$

and integration parameters chosen with $\beta = 1/4, \gamma = 1/2$ as a necessary requirement for numerical stability. The system of algebraic equations (17) nonlinearly depending on $\boldsymbol{U}^i$ may be solved with a Newton-Raphson method while proceeding time step by time step.

This completes the discretization. Application examples for wave propagation problems and plane strain beams under impact actions are described in [7]. Two special cases will be considered in the following: propagation of a uniaxial tensile wave along a bar to discuss dynamic strength increase factors and reflection of a uniaxial compressive wave at a bar's end as tensile wave leading to spallation to discuss aspects of dynamic crack energy.

4 UNIAXIAL TENSILE WAVE PROPAGATION

We consider a linear elastic bar with Young's modulus E and a specific mass ϱ exposed to uniaxial wave propagation. Its left end is given with a coordinate $x = 0$ and a right end with $x = L$ and $L = 1m$. A discretization with for node axis symmetric plane elements with an element length of $L_e = 3mm$ and a time step according to the wave speed within the element $\Delta t = 0.7 \cdot 10^{-3} ms$ is chosen for the for the numerical computations. Aspects of an appropriate selection are discussed in [7].

A tensile stress wave with a constant strain rate $\dot{\epsilon}_0$ is induced on the left end with prescribing the left end displacement u_0 depending on time t

$$u_0(t) = -\frac{1}{2}\,\dot{\epsilon}_0\, c \cdot t^2, \quad t \geq 0 \tag{23}$$

with a uniaxial wave speed $c = \sqrt{E/\varrho}$ leading to a left end stress

$$\sigma = E\,\dot{\epsilon}_0 \cdot t \tag{24}$$

A sequence of stress waves along the bar for several times is shown in Fig. 3 for $E = 36000\,\text{MN/m}^2$, $\varrho = 24\,\text{kN/m}^3$ for a concrete grade C40 according to [3] and $\dot{\epsilon}_0 = 1\,\text{s}^{-1}$. The linear elastic stress waves are characterized by a constant slope according to the prescribed strain rate $\dot{\epsilon}_0$. The tensile strength of concrete will obiviously be reached after a short period.

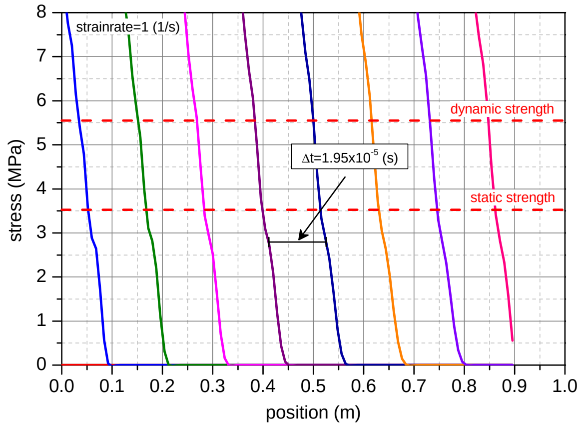

Figure 3: Linear elastic tensile wave propagation with constant strain rate $\dot{\epsilon} = 1\,\mathrm{s}^{-1}$.

The course of stress waves changes if a nonlinear material behavior with limited strength is assumed according to Section 2. An example is given with Fig. 4 where the Visco-Elastic Retarded Damage approach (VERD) was used for the same concrete grade as before with material strain rate parameters $m_\kappa = 1 \cdot 10^{-12} s^2, E_2 = E, \eta_2 = 2.8 \cdot 10^{-8}$.

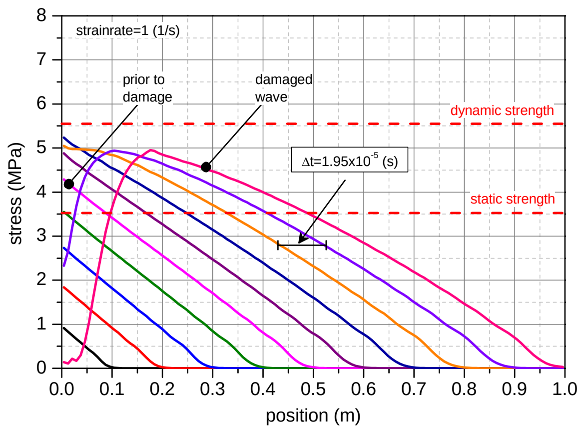

Figure 4: Nonlinear tensile wave propagation (VERD) with constant strain rate $\dot{\epsilon} = 1\,\mathrm{s}^{-1}$.

This starts with the same behavior as in the linear elastic case. The initial linear elastic state is followed by a nonlinear hardening state whereby tensile stresses considerably exceed the quasi static tensile strength $f_{ct} = 5.5\,\mathrm{MN/m}^2$ due to viscosity and gradient retarded damage. The material achieves a maximum dynamic tension and switches into the softening branch.

These basically applies to all material points along the bar but at different times and with a different extent due to nonlinear wave propagation. Furthermore, the actually achieved strain rates apart from the left bar end differ from the prescribed nominal value $\dot{\epsilon}_0$ because of the nonlinear material behavior. Finally, a strain localization occurs in the left end bar region with maximum values at $x = 0$. This is mesh independent due to the regularization approach. Using this setup a variety of associated values of stress, strain and strain rate can be determined.

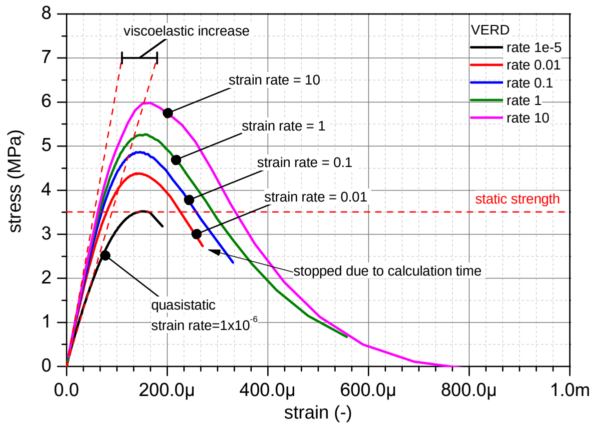

Figure 5: Uniaxial stress-strain relations (VERD) at different strain rates.

This leads to uniaxial stress-strain curves which are parametrized by the strain rate. Examples are shown in Fig. 5 for the viscoelastic retarded damage approach (VERD). First of all, a higher stress i.e. a higher strength exceeding the quasi static tensile strength is reached for higher strain rates. Furthermore, the initial Young's modulus also increases due to the activation of the additional stiffness E_2 in case of higher strain rates, see Fig. 1 'Maxwell'.

For a comparison the computed uniaxial stress-strain curves for retarded damage without viscosity (ERD) are shown in Fig. 6. The achieved stresses are lower for the same strain rate compared to VERD but still considerably exceed the quasi static tensile strength. On the other hand, the initial Young's modulus remains unchanged as no additional stiffness is activated with the material model according to Fig. 2 alone. Experimental data which might validate this particular effect are rare and show a large scatter.

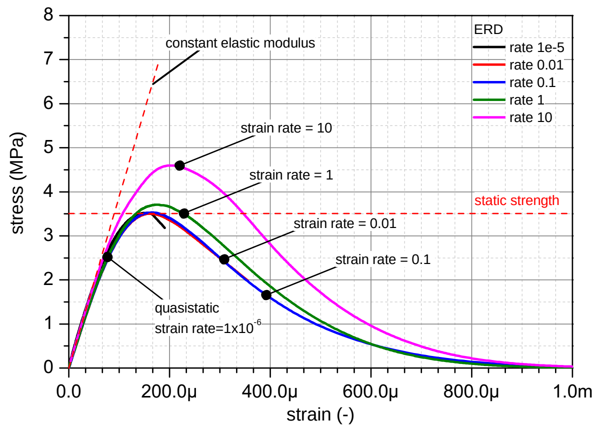

Figure 6: Uniaxial stress-strain relations (ERD) at different strain rates.

More credible experimental data are available for the maximum achieved tensile stress or dynamic tensile strength, respectively, varying with the strain rate. This leads to the dynamic strength increase factor (DIF) as the relation between dynamic strength and quasistatic strength depending on the strain rate.

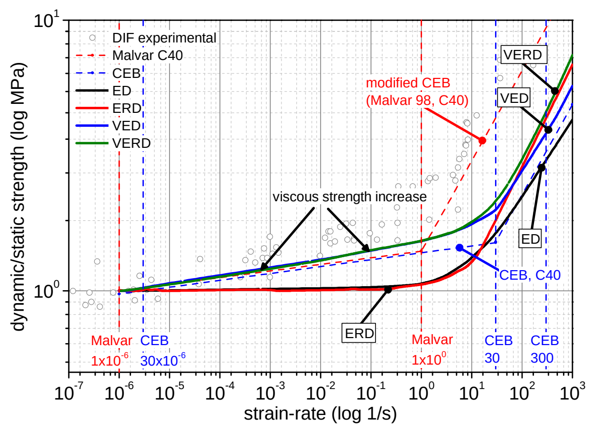

Figure 7: Experimental and computed dynamic tensile strength increase factors.

A comparison of experimental and computed DIF-data is shown in Fig. 7 in a double logarithmic scale. Approximately a bilinear course is given. The dynamic material parameters were chosen with the same values as before. This choice approximately reproduces the DIF-recommendations of the CEB-Modelcode [3] with the computed values. Other choices might lead to a better approximation of experimental values.

5 SPALLATION

5.1 Basic relations

Up to now the variations of strength and Young's modulus were discussed under high strain rate conditions. Another issue concerns the crack energy. Crack energy may be defined as energy dissipated in the process of macro crack creation. This energy is widely accepted as material constant under quasi static conditions.

An appropriate setup to determine the crack energy under high strain rate condition is given by the spallation experiment. A uniaxial compressive stress wave is induced on the left end of a bar of length L. It is assumed as half sine shaped and its maximum stress value is far below the compressive strength but considerably above the tensile strength. On the right end it is reflected as tensile wave. In case of linear elastic wave propagation the reflection process is characterized by stress shapes as shown in Fig. 8, i.e. upon reaching the right end the stress amplitude reduces, goes through zero and increases to its original value with reversed sign.

During the reflection process the right end of the bar, which initially has a zero displacement, is moved to the right. The associated velocity is shown in Fig. 9 varying with the same time t. The time of the maximum velocity corresponds to the time when the stress wave passes through zero, see Fig. 8. Upon velocity reduction the amplitude of the stress wave increases as has been described before. Thus, a relation can be derived between velocity reduction and stress amplitude.

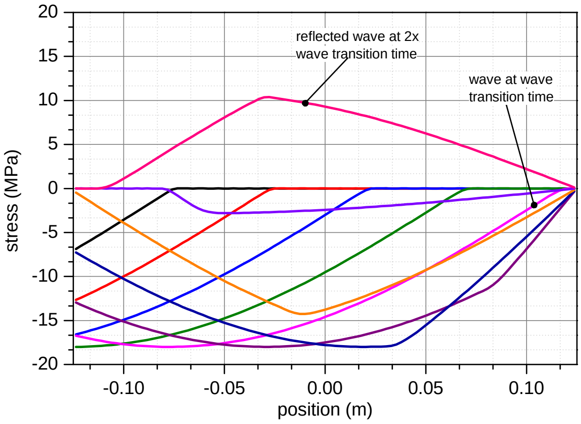

Figure 8: Reflection of compressive stress wave as tensile wave on free end.

Such a relation basically also holds in case of a material with limited tensile strength. In case when the tensile stress wave amplitude reaches the uniaxial tensile strength a fragment of the bar will break apart on the right end and will start to fly away in the right direction. This occurs at a time t_1 whose value is needed for later calculations. The velocity of the right end of the fragment will than stop its decelaration and holds some remaining value, see Fig. 9.

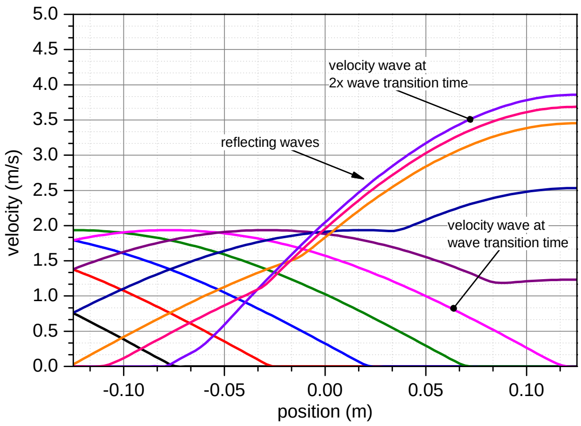

Figure 9: Reflection of velocity wave on free end.

The absolute difference between this value and the maximum velocity is called pull-back-velocity Δv_{vp}. A relation between the pull-back-velocity and the corresponding stress amplitude or dynamic uniaxial tensile strength $f_{t,d}$ is given by

$$f_{t,d} = \frac{1}{2}\,\varrho\, c\, \Delta v_{vp} \tag{25}$$

with the specific mass ϱ and the wave speed c. This relation serves to determine values of the dynamic tensile strength $f_{t,d}$ in spallation experiments.

Assuming a linear elastic tensile behavior up to the moment t_1 of tensile failure for a given stress wave and given value Δv_{vp} also allows to calculate the spatial point x_1 where the failure occurs, i.e. the fragment length. Furthermore, the velocity $v(x,t)$ along the fragment may be computed for the time t_1 leading to an impulse

$$\begin{aligned} I_1 &= \int_{x_1}^{L} v(x,t_1)\,\varrho A \mathrm{d}x \\ &\approx \frac{1}{2}\varrho A(L-x_1)\,[v(x_1,t_1)+v(L,t_1)] \end{aligned} \tag{26}$$

A analogous relation holds for a later time t_2 when a macro crack has fully developed in the cross section x_1 leading to an impulse I_2.

During the spallation process a stress σ is transmitted over the cracked cross section due to the formation of a crack band and the softening stress-strain behavior of the material. This is related to the difference of impuls by

$$\int_{t_1}^{t_2} \sigma\, A\mathrm{d}t = I_1 - I_2 = \Delta I \tag{27}$$

The stress starts with the dynamic tensile strength $f_{t,d}$ and ends up with zero after the formation of a macro crack. On the other hand, stress and crack energy are connected by

$$\begin{aligned} G_{f,d} &= \int_0^{\delta_2} \sigma\, A\mathrm{d}\delta \\ &= \int_0^{t_2} \sigma\dot{\delta}\, A\mathrm{d}t \approx \dot{\delta}_{mean} \int_0^{t_2} \sigma\, A\mathrm{d}t \end{aligned} \tag{28}$$

with a variable crack width δ, a crack width δ_2 at time t_2 and the crack width velocity $\dot{\delta}$. This leads to

$$G_{d,f} = \dot{\delta}_{mean}\, \Delta I \tag{29}$$

Finally, the velocity of the crack width remains to be determined. It is derived from the velocity of the fragment's left end

$$\dot{\delta}(t) = v(x_1,t) - v(x_1,t_1) \tag{30}$$

The mean velocity may be approximated by

$$\dot{\delta}(t)_{mean} \approx \frac{1}{2}\left[\dot{\delta}(t_2) + \dot{\delta}(t_1)\right] = \frac{1}{2}\,\dot{\delta}(t_2) \quad (31)$$

This completes a method which allows the experimental determination of the high strain rate crack energy from measured values of velocities [13]. It bases on the knowledge of the stress wave. This may be determined in a Hopkinson-Bar setup with the specimen connected to an incident bar only. Furthermore, a linear elastic behavior up to the point of tensile failure is assumed.

Whether this assumption is valid may to some degree be controlled by comparing the measured fragment length and the theoretical length $L - x_1$. Moreover, this method relies on correctly measured velocities which may be achieved with high speed cameras.

A somehow crucial point exists with the determination of the time t_2, i.e. the time when the crack has fully developed to become a macro crack and does not transmit stresses anymore.

5.2 Computational results

Computational methods provide, e.g., stresses which are not or not directly accessible to experimental measurement. But such methods at least require an assumption about material models and the specification of their parameters.

The method as it has been described in the previous section may serve to link experimental investigations and numerical simulations.

The proposed material formulation and the numerical method are applied to a spallation test simulation. An axisymmetric formulation is used to describe a long cylindrical specimen according to the experimental setup in [13].

The specimen of 0.250 m length and 0.075 m diameter was discretized with 1485 axisymmetric four node square elements which leads to approx. 2.5 mm mesh size.

The specimen was pressure loaded from the left end with a half sine wave of amplitude 18 MPa and 0.1 ms duration. It is free in motion and a wave reflection occurs at the right end.

The time step of the Newmark method was chosen according to explicit solution methods with 0.8 of the maximum wave transition time within an element.

A C40 concrete parameter set was considered according to Section 4 which leads to a wave transition time through the specimen of 65 μs and a time step size of 0.5 μs. The Poisson's ratio is assumed with 0 to avoid spurious secondary waves.

Fig. 10 illustrates the stress distribution along the specimen at different time steps for the VERD material formulation. The pressure wave is travelling through the specimen and reflects at the free end into a tensile wave moving back. (see section 5.1).

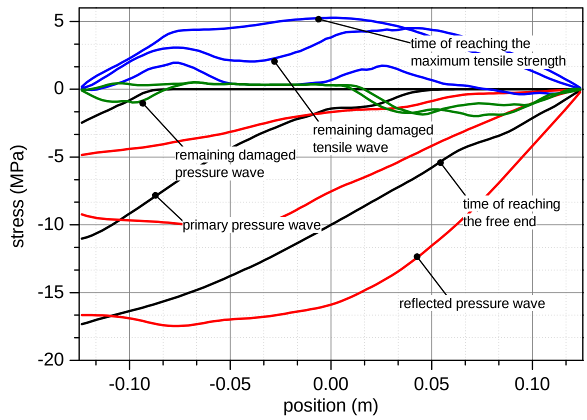

Figure 10: Stress wave distribution along the specimens center axis.

The tensile wave amplitude exceeds the strength of the material and tensile damage occurs nearly at the center of the specimen according to the incoming impulse length.

The specimen than spalls at this position into two separate pieces while the remaining internal stress waves are still propagating and reflecting in both parts.

Fig. 11 shows the corresponding displacement distribution at different time steps. The spallation time is reached at 110 μs with the initiation of the separation.

The mean speed of the left part with 1.38 m/sec is less than 1.89 m/sec for the right part at this time and the secondary part will fly away.

The softening process takes approximately 30 μs, after this time the specimen is fully separated with the remaining mean part velocities of 2.13 m/s and 1,96 m/s. This indicates a gap between both.

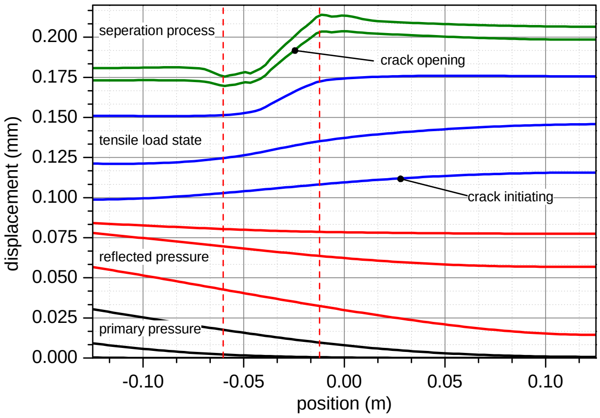

Figure 11: Corresponding displacement distribution.

The corresponding local strain distribution is illustrated in Fig. 12 and shows a widely spanned zone between both parts. At the position -0.04 m a strain peaks can be recognized as a strong starting localization in this area leading to a "separation" at the respective element. This is a well known numerical effect due to missing regularization and does not reflect some physical behavior. To avoid this effect the damage formulation is coupled to a nonlocal strain variable as introduced in Section 2.3.

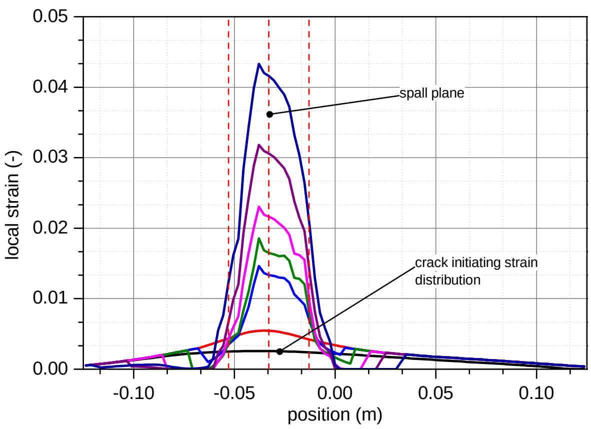

Figure 12: Local strain distribution.

The corresponding nonlocal strain distribution is shown in Fig. 13 at the same time steps. One can see that the regularization procedure smoothes the maximum strain values. The maximum strain can now be recognized at approximately x=-0.03 m at the left side from the center of Fig. 13.

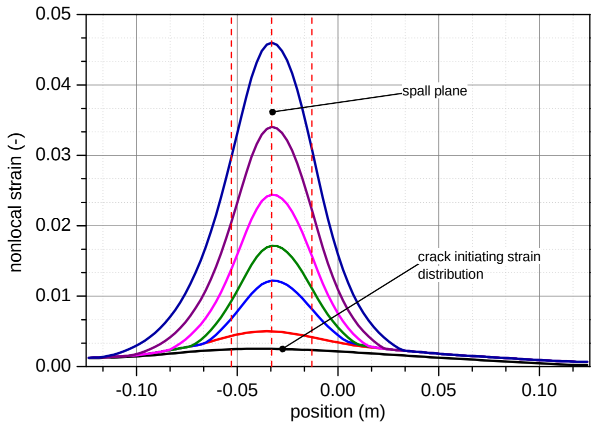

Figure 13: Nonlocal strain distribution.

The spallation plane is located at the position of maximum strain and leads to two parts of 84 mm and 166 mm length. Using Eq. (25) the tensile strength is calculated with 4.3 MPa with a pullback velocity $\Delta v_{vp} = 0.78$ m/sec. Furthermore, the knowledge of the separation plane and the masses of the remaining pieces allows for calculating the dynamic crack energy from the transferred impulse by Eq. (29). In this particular case the dynamic crack energy 27 N/m is much less than the expected experimental value according to [13] of approximately 150 N/m. The difference is probably caused by the assumed viscous damage evolution and regularization parameters which are based on quasi static experimental data. Especially this last issue needs more investigations.

A computed stress-strain relation is shown in Fig. 14 for the most damaged element. It has the regimes of (1) the compressive load for the incident pressure wave, followed by (2) the unloading branch due to the wave reflection with reversal to tension. It reaches the tensile strength at (3) followed by a softening part and is again (4) unloading the not fully damaged material. It undergoes further a secondary compressive load at

(5) with reaching the maximum stress at (6) and again softens at the compressive domain (7) to full damage, which finally leads to (8) the large straining part which indicates the gap.

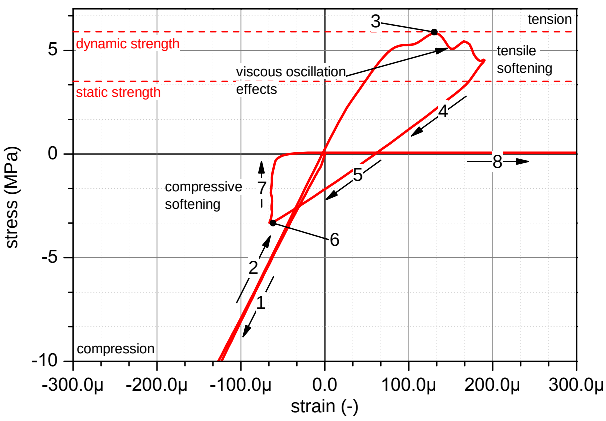

Figure 14: Stress strain evolution of the most damaged element of the VERD model.

The assumption of a constant homogeneous wave traveling through the specimen introducing a ductile crack at a predefined position, underlies all experimental investigations. This might be insufficient as it is indicated by the numerical simulations. Fig. 15 shows the evolution of the strain-rate with time at different positions. The strain-rate is not constant as assumed in experimental observations and rather shows varying values during the cracking process.

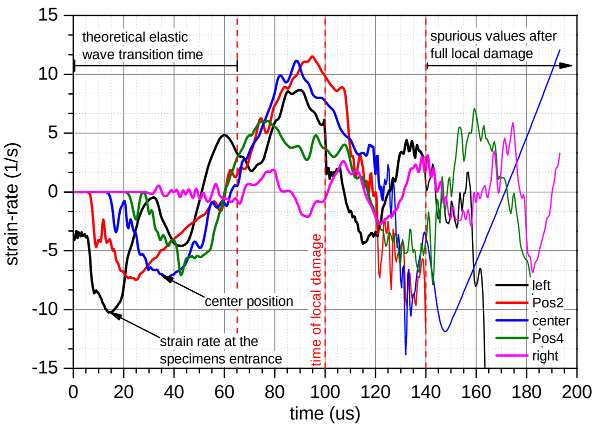

Figure 15: Strain rates distribution at different positions.

If the strain-rate varies with time and position the local strength will be different depending on both. The viscous and the retardation part of the material model introduce this strain-rate variation leading to the inhomogeneous damage within the specimen. The strain-rate for this particular simulation with the VERD formulation spans from 18 1/s to 24 1/s during the main cracking process instead of 30 1/s for purely linear elastic considerations.

These prior observations were made with the VERD material formulation leading to time and space dependent damage behavior as described before. Additionally, Fig. 16 compares the stress evolution at some representative positions for the linear elastic (E) and the visco-elastic (VE) material model without damage.

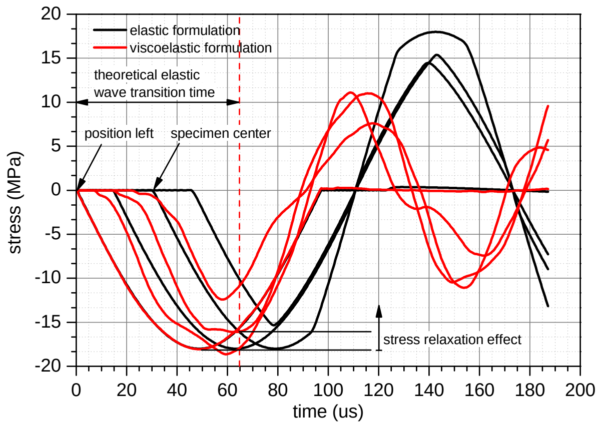

Figure 16: Stress distribution at 4 different positions for the E and VE formulation.

The viscous part increases the elastic stiffness with increasing strain-rate. Thus, the wave speed increases and the traveling time through the specimen reduces. The dynamic elastic modulus increases from 36 GPa for the linear elastic case to 50 GPa for the visco-elastic case and the wave speed increases to 4677 m/sec as mean value of the specimen. Furthermore, it can be seen that the viscous stress evolution varies with the position. The stress wave changes in shape and speed. This probably leads to some overlaid inhomogeneous bouncing with time and the observed oscillation.

The same effect can be recognized by introducing the damage part according to the elastic damage model (ED), the visco-elastic damage model (VED), the retarded damage model without (ERD) and with viscous part (VERD), see Fig. 17.

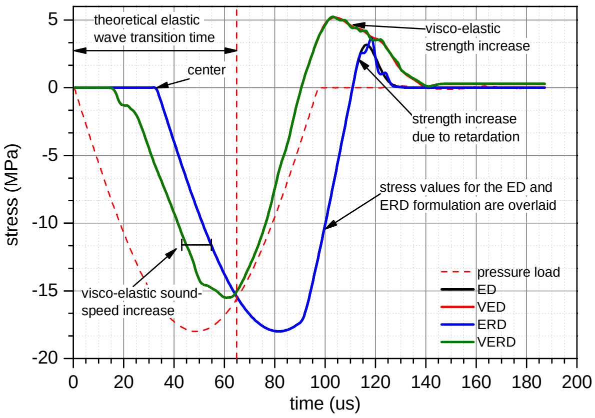

Figure 17: Stress distribution at the center of the specimen for the 4 damaged formulations.

The elastic (ED) formulation reacts with a maximum tensile strength equal to the static assumption of approx. 3.5 MPa while the viscous (VED) one increase to 4.3 MPa. The corresponding mean strain rate reduces in this case from 30 1/s to 11 1/s. Introducing the damage retardation part, the viscous influence remains unchanged and the same kind of oscillation can be found as has been described before.

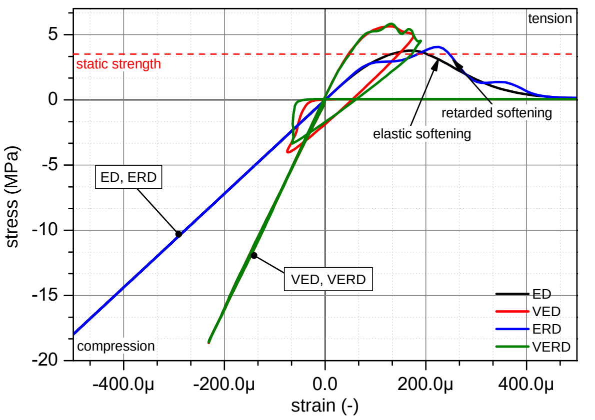

Figure 18: Overlaid stress strain relation for the 4 damaged formulation.

The superimposed stress-strain relations in Fig. 18 for the position with the largest stress values may explain this effect more clearly. The none-viscous formulations react with a full separation in the tensile domain which corresponds to a brittle behavior.

The viscous contributions on the other hand lead to a more bearable strength in tension and a not fully damaged state during the first unloading branch. Full damage is finally reached in the next loading cycle in the compressive domain.

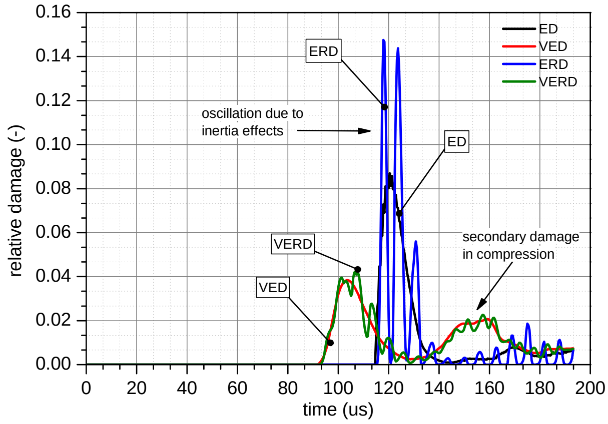

Figure 19: Relative damage.

This behavior can be summarized with introducing a global differential damage evolution parameter stepwise holding the actual damage increase. Fig. 19 compares this parameter for the four damage formulations. It can be seen, that the non-viscous formulations react with a short high damage rate and the viscous formulations with a lower, more ductile first part, followed by the secondary damage increase.

6 CONCLUSIONS

A novel material model with viscoelastic retarded damage is discussed in this paper. The viscous part of the formulation leads to a moderate strength increase with increasing strain rate at lower values up to approx. 1 1/s. The retardation part assumes crack opening inertia effects at higher rates and significantly increases the virtual strength in this domain. While the formulation of the stress-strain relations is fully triaxial the model is applied to particular case of uniaxial wave propagation. The three material parameters may be calibrated such that the typical course of dynamic strength increase factors as given by recommendations and experimental investigations may be approximated to a desired degree. Numerical simulations of spallation experiments exhibit some discrepancies to experimental investigations. On one hand these discrepancies have to be contributed to an improvable parameter calibration of the material model, on the other hand the simulations reveal complex spallation mechanisms which seem not to be adequately regarded in the setup and processing of spallation experiments.

REFERENCES

[1] F. Barpi. Impact behaviour of concrete: a computational approach. *Engineering Fracture Mechanics*, 71:2197–2213, 2004.

[2] P.H. Bischoff and S.H. Perry. Compressive behavior of concrete at high strain rates. *Materials and Structures*, 24:425–450, 1991.

[3] Comite Euro-International de Beton. *CEB-FIP Model Code 1990*. Thomas Telford, London, 1993.

[4] J. Eibl and B. Schmidt-Hurtienne. Strain-rate-sensitive constitutive law for concrete. *Journal of Engineering Mechanics,*, 125:1411–1420, 1999.

[5] U. Häussler-Combe and J. Hartig. Formulation and numerical implementation of a constitutive law for concretewith strain-based damage and plasticity. *International Journal of Non-Linear Mechanics*, 43:399–415, 2008.

[6] U. Häussler-Combe and M. Kitzig. Modeling of concrete behavior under high strain rates with inertially retardeddamage. *International Journal of Impact Engineering*, 36:1106–1115, 2009.

[7] U. Häussler-Combe and T. Kuehn. Modeling of strain rate effects for concrete with viscoelasticity and retardeddamage. *International Journal of Impact Engineering*, 2012.

[8] T. Holmquist, G. Johnson, and W. Cook. A computational constitutive model for concrete subjected to high strainrates and high pressures. In *Proc. 14th International Symposisum on Ballistics.*, pages 591–600, Quebec, 1993.

[9] L. J. Malvar and C. A. Ross. Review of strain rate effects for concrete in tension. *ACI Materials Journal*, 95:735–739, 1998.

[10] L. E. Malvern. *Introduction to the Mechanics of a Continuous Medium*. Prentice-Hall, Englewood Cliffs, New Jersey, 1. auflage edition, 1969.

[11] H. W. Reinhardt and J. Weerheijm. Tensile fracture of concrete at high loading rates taking account of inertiaand crack velocity effects. *International Journal of Fracture*, 51:31–42, 1991.

[12] P. Rossi. A physical phenomenon which can explain the mechanical behaviour of concreteunder high strain rates. *Materials and Structures*, 24:422–424, 1991.

[13] H. Schuler, Ch. Mayrhofer, and K. Thoma. Spall experiments for the measurement of the tensile strength and fractureenergy of concrete at high strain rates. *International Journal of Impact Engineering*, 32:1635–1650, 2006.

[14] A. Suffis, T. A. A. Lubrecht, and A. Combescure. Damage model with delay effect: Analytical and numerical studies of theevolution of the characteristic damage length. *International Journal of Solids and Structures*, 40:3463–3476, 2003.